Supporting Information for

Binucleating Jäger-type $\{(N_2O_2)_2\}^{4-}$ ligands: Magnetic and electronic interactions of Fe(II), Ni(II) and Cu(II) across an in-plane TTF-bridge

Constantin Schreck,[a] Sophie Schönfeld,[a†] Phil Liebing,[b] Gerald Hörner [b] and Birgit Weber*[b]

[a.] *Department of Chemistry, Inorganic Chemistry IV, University of Bayreuth, 95447 Bayreuth, Germany.*

[b.] *Institute for Inorganic and Analytical Chemistry, Faculty of Chemistry and Earth Sciences, Friedrich-Schiller-University Jena, Germany.*

† Present Address: Fraunhofer Institute for Environmental, Safety and Energy Technology UMSICHT, Institute Branch Sulzbach-Rosenberg, Department Renewable Energy, 92237 Sulzbach Rosenberg.

^{1}H-NMR spectra

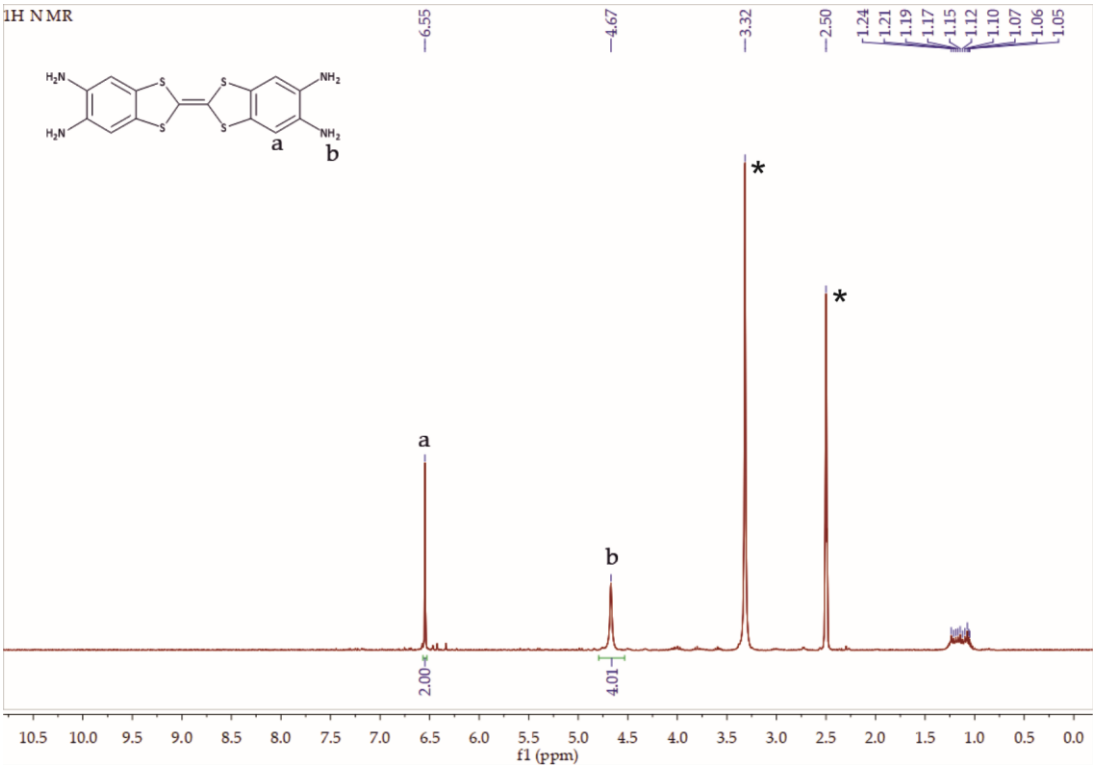

Figure S1: ^{1}H-NMR spectrum of ligand precursor **2** in dmso-d_6 (300 mHz) with signal assignments. Solvent signals are marked with *.

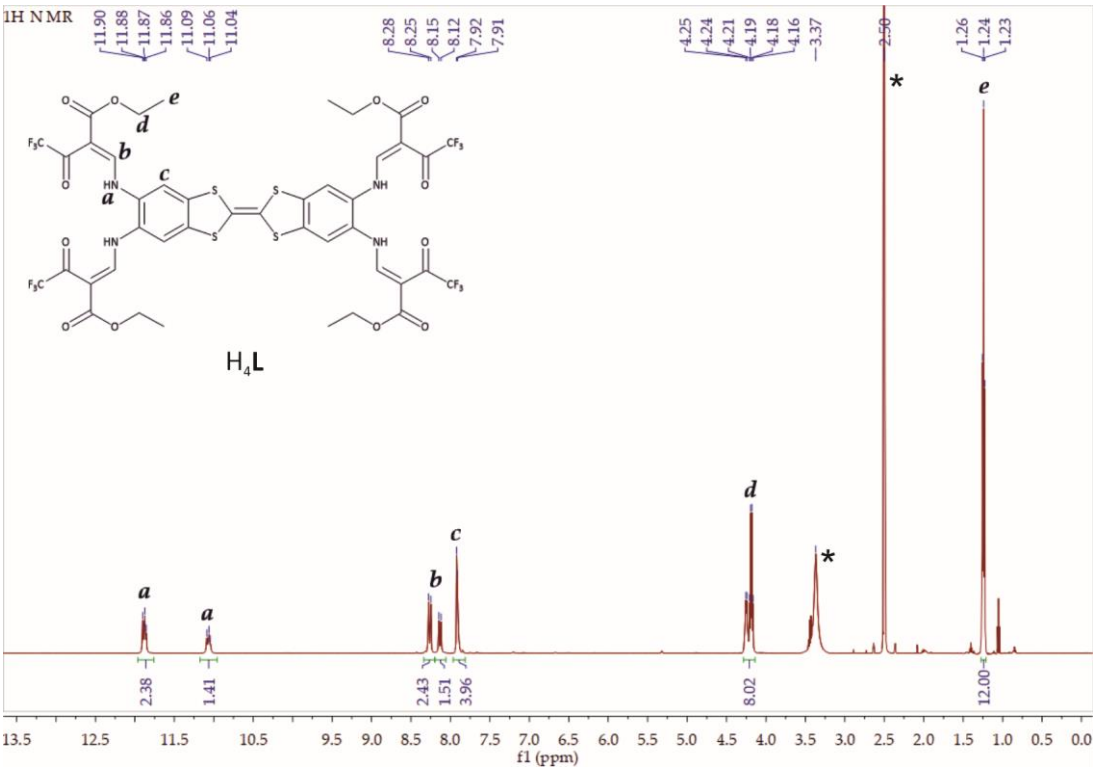

Figure S2: ^{1}H-NMR spectrum of ligand H_4**L** in dmso-d_6 (500 mHz) with signal assignments. Solvent signals are marked with *.

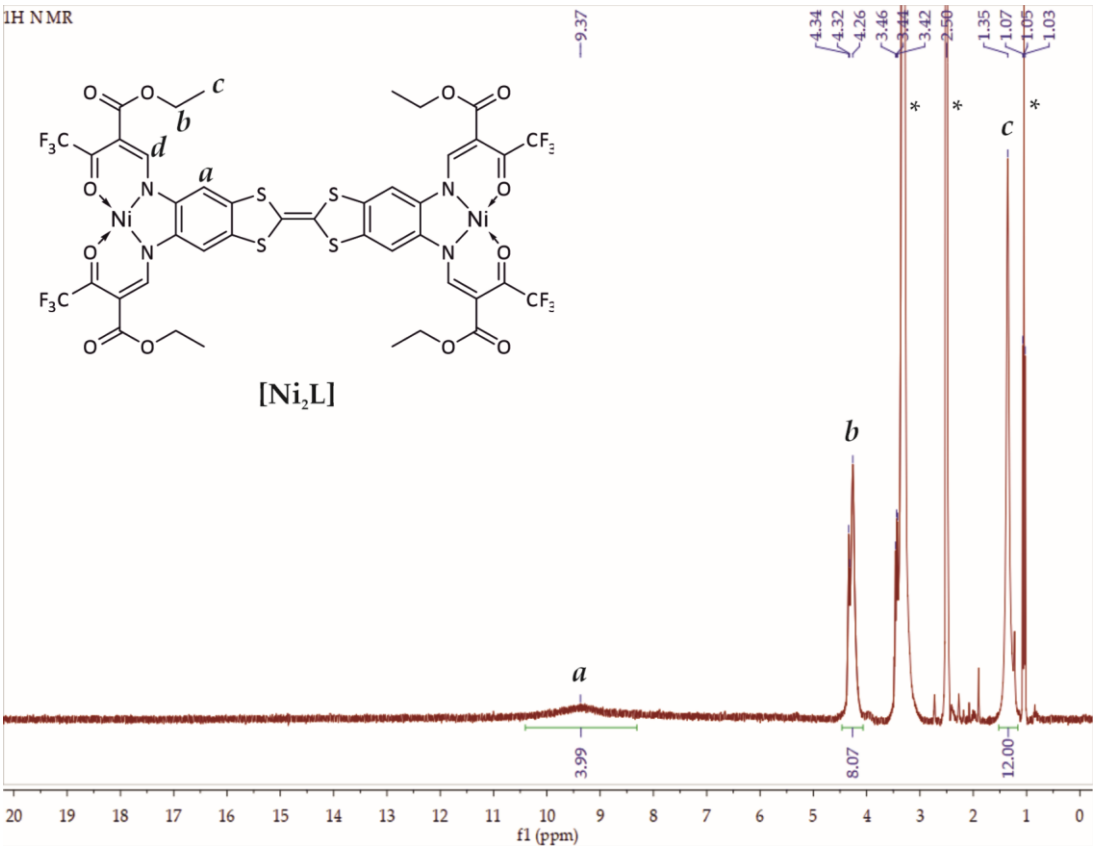

Figure S3: ^{1}H-NMR spectrum of **[Ni$_2$L]** in dmso-d$_6$ (500 mHz) with signal assignments. Solvent signals (dmso, H_2O and EtOH) are marked with *****.

Mass spectrum

ESI neg: H_4**L** in MeCN

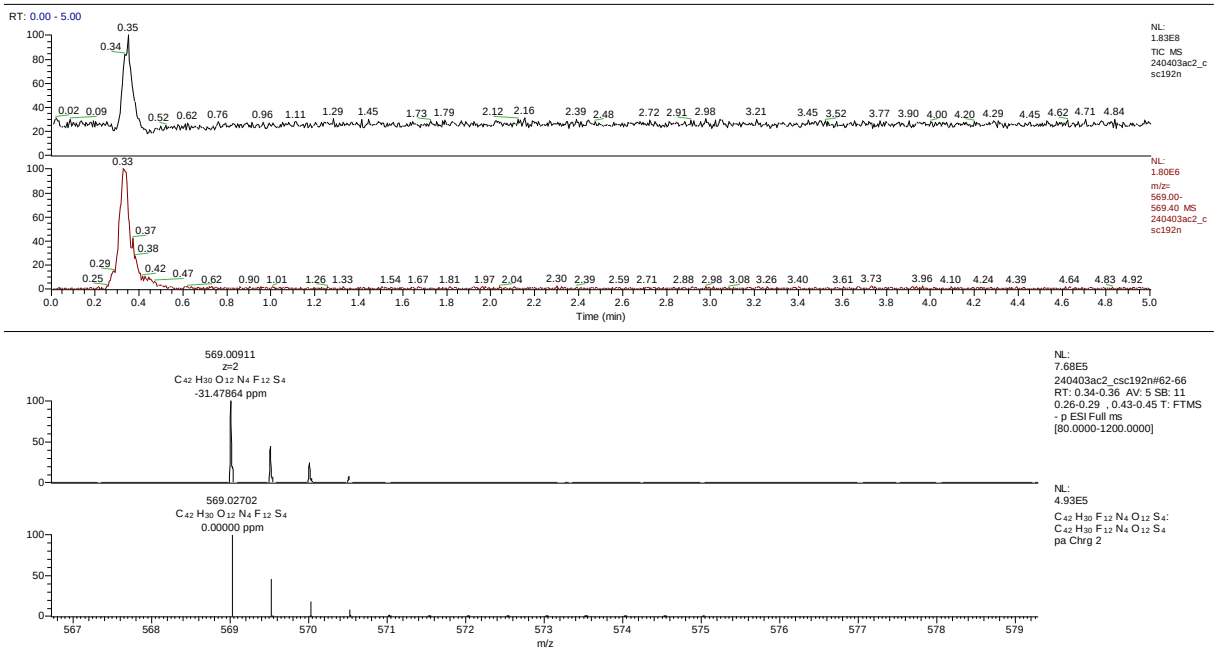

Figure S 4: Mass spectrum of H_4**L** in MeCN.

IR spectra

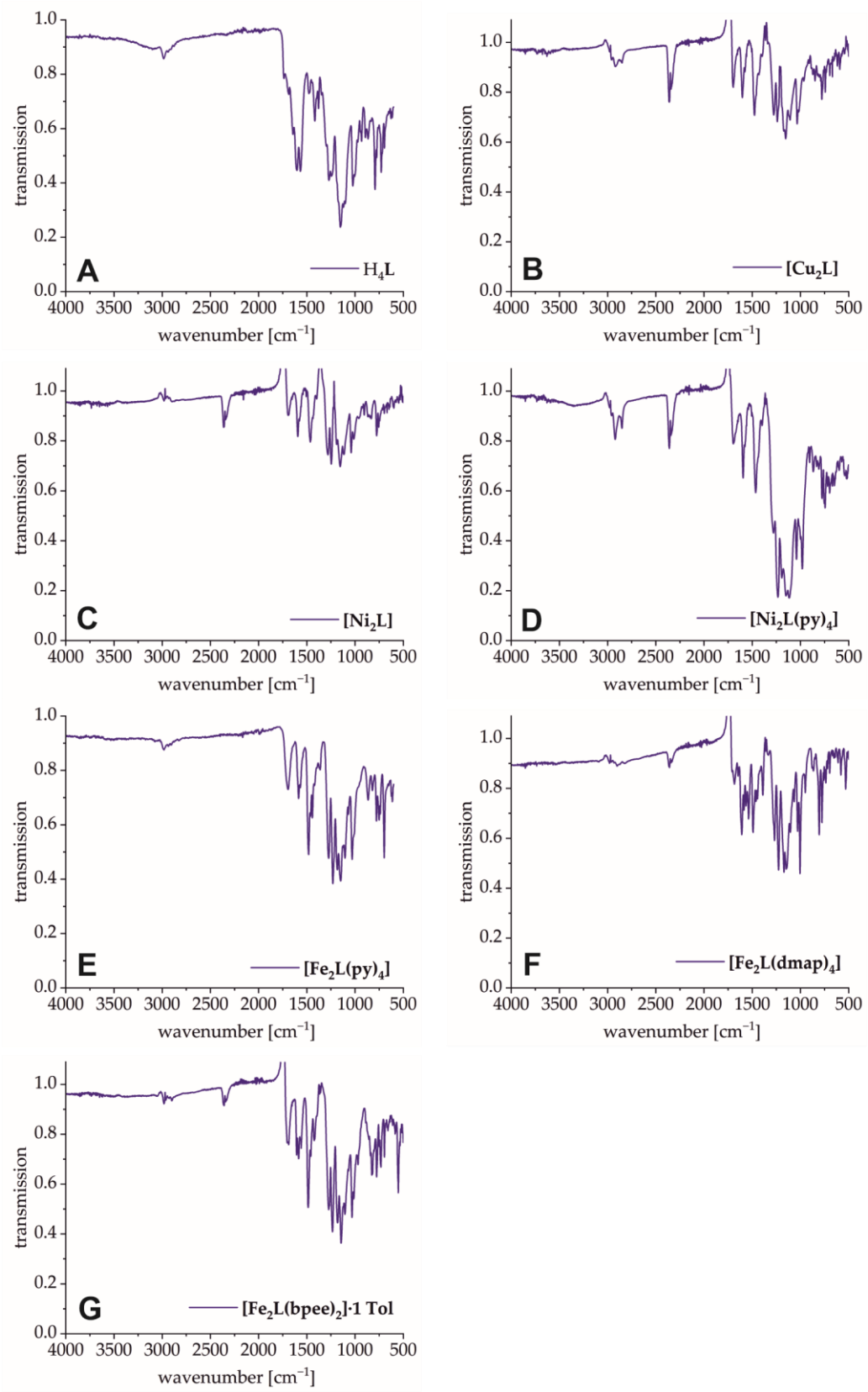

Figure S5: FT-IR spectrum of (**A**) H_4**L**, (**B**) **[Cu_2L]**, (**C**) **[Ni_2L]**, (**D**) **[Ni_2L(py)$_4$]**, (**E**) **[Fe_2L(py)$_4$]**, (**F**) **[Fe_2L(dmap)$_4$]** and (**G**) **[Fe_2L(bpee)$_2$]·1 Tol.**

Cristallographic data

Table S1: Crystallographic data of **[$Ni_2L(py)_4$]**.

Compound	**[$Ni_2L(py)_4$]**
CCDC number	2332706
Formula	$C_{62}H_{48}F_{12}N_8Ni_2O_{12}S_4$ [+ solvent]
Crystal size [mm]	0.054 × 0.051 × 0.041
Crystal description	Red platelet
M [g mol^{-1}]	1570.74
T [K]	180 K
λ [nm]	0.71073
Crystal system	tetragonal
Space group	$P4_2$
a [Å]	17.8926(3)
b [Å]	17.8926(3)
c [Å]	24.3239(5)
α [°]	90.0
β [°]	90.0
γ [°]	90.0
V [Å^3]	7787.2(3)
Z	4
$\rho_{calculated}$ [mg cm^{-3}]	1.429
μ [mm^{-1}]	0.684
F(000)	3200
Θ_{range} [°]	1.8–29.0
Reflections collected	34757
Indep. reflections (R_{int})	16403 (0.050)
*R*1	0.0572
w*R*2	0.1447
GooF (S)	0.938
Min. and Max. $\rho_{residual}$ [e Å^{-1}]	−0.40, 1.01

Table S2: Selected bond lengths and bond angles of **[$Ni_2L(py)_4$]**.

[$Ni_2L(py)_4$]			
	Bond length [Å]		Bond angles [°]
d(Ni1–N1)	1.991(7)	∡(N1–Ni1–O4)	168.6(3)
d(Ni1–N2)	2.008(7)	∡(N2–Ni1–O3)	172.7(2)
d(Ni1–O3)	2.020(5)	∡(N5–Ni1–N6)	174.7(3)
d(Ni1–O4)	2.065(6)	∡(O3–Ni1–O4)	100.6(2)
d(Ni1–N5)	2.117(7)	∡(N3–Ni2–O10)	173.7(2)
d(Ni1–N6)	2.151(7)	∡(N4–Ni2–O9)	173.8(3)
d(Ni2–N3)	1.961(6)	∡(N7–Ni2–N8)	176.8(3)
d(Ni2–N4)	2.009(6)	∡(O9–Ni2–O10)	96.1(2)
d(Ni2–O9)	2.010(6)		
d(Ni2–O10]	2.039(5)		
d(Ni2–N7)	2.139(7)		
d(Ni2–N8)	2.198(7)		
d(C21–C22)	1.345(11)		

Table S3: Selected distances for short contact F···F interactions in **[$Ni_2L(py)_4$]**.

	Distance [Å]
d(F2–F8)	2.867(8)
d(F3–F12)	2.839(7)
d(F4–F11)	2.784(9)

Table S4: Distances and angles of the aromatic interactions within **[$Ni_2L(py)_4$]**. Cg(I) and Cg(j) are the centroids. Given are the angles between the ring planes, the perpendicular distance between the gravitational center and the respective ring as well as the slippage

Cg(I)	Cg(J)	Cg(I)–Cg(J) [Å]	*α* [°]	*β* [°]	*γ* [°]	Cg(I)-perp [Å]	Cg(J)-perp [Å]	Slippage [Å]
S1 – C19 – C20 – S2 – C21	N7 – C53 – C54 – C55 – C56 – C57	3.814(5)	16.1(4)	12.3	27.2	3.393(3)	3.726(4)	0.814
S3 – C22 – S4 – C24 – C23	N6 – C48 – C49 – C50 – C51 – C52	3.843(5)	17.8(4)	13.4	29.4	3.347(3)	3.739(4)	0.888
N5 – C43 – C44 – C45 – C46 – C47	N5 – C43 – C44 – C45 – C46 – C47	3.658(6)	11.5(5)	13.5	13.5	3.556(4)	3.557(4)	0.853
N6 – C48 – C49 – C50 – C51 – C52	S3 – C22 – S4 – C24 – C23	3.843(5)	17.8(4)	29.4	13.4	3.739(4)	3.347(3)	1.889
N6 – C48 – C49 – C50 – C51 – C52	C23 – C24 – C26 – C28 – C27 – C25	4.183(5)	18.9(4)	40.7	26.2	3.755(4)	3.171(3)	2.729
N7 – C53 – C54 – C55 – C56 – C57	S1 – C19 – C20 – S2 – C21	3.814(5)	16.1(4)	27.2	12.3	3.726(4)	3.393(3)	1.742
N7 – C53 – C54 – C55 – C56 – C57	C15 – C16 – C18 – C20 – C19 – C17	4.096(5)	17.6(4)	35.3	23.7	3.751(4)	3.344(3)	2.366
N8 – C58 – C59 – C60 – C61 – C62	N8 – C58 – C59 – C60 – C61 – C62	3.794(5)	18.4(4)	16.1	16.1	3.646(4)	3.645(4)	1.052
C15 – C16 – C18 – C20 – C19 – C17	N7 – C53 – C54 – C55 – C56 – C57	4.096(5)	17.6(4)	23.7	35.3	3.344(3)	3.750(4)	1.647
C23 – C24 – C26 – C28 – C27 – C25	N6 – C48 – C49 – C50 – C51 – C52	4.184(5)	18.9(4)	26.2	40.7	3.171(3)	3.756(4)	1.844

DFT-Modelling frontier orbital pattern

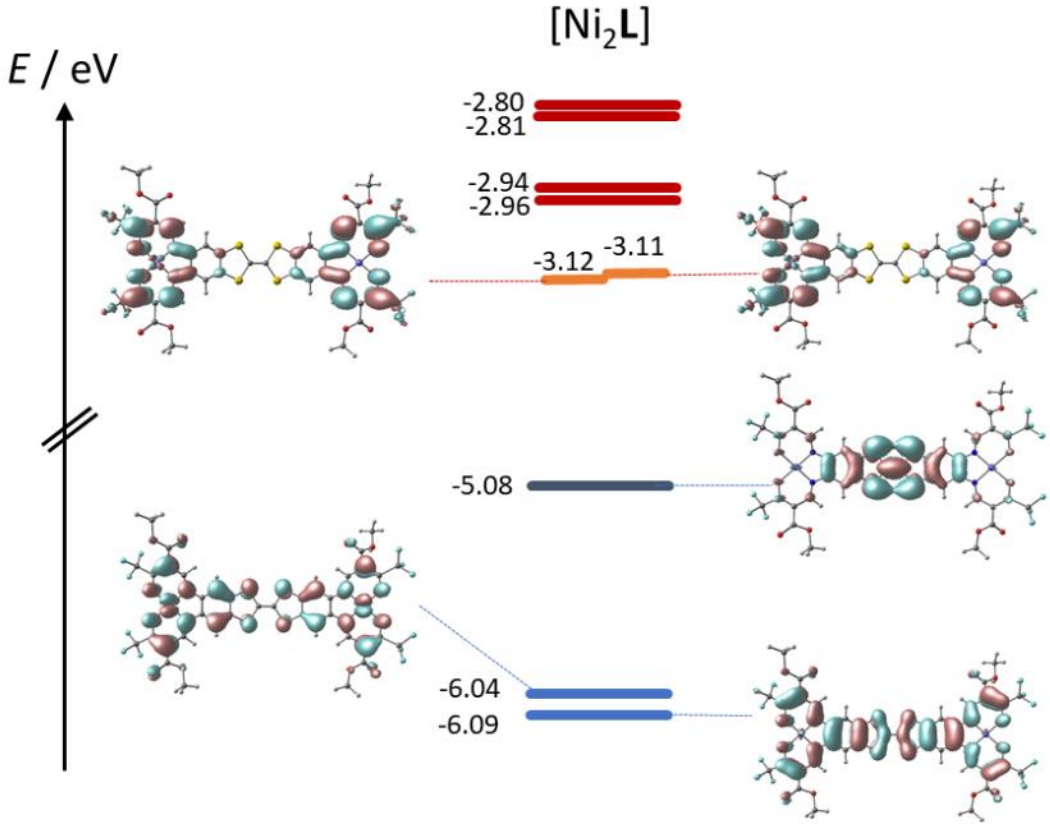

Figure S6: Kohn-Sham frontier MO energy diagram and orbital plots of the binuclear nickel complex **[Ni_2L]**.

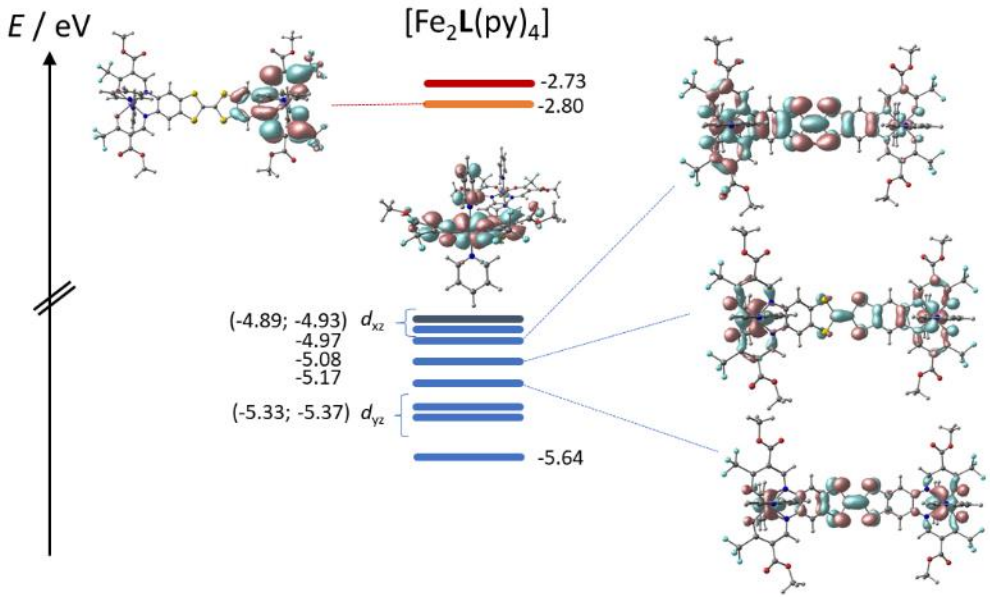

Figure S7: Kohn-Sham frontier MO energy diagram and orbital plots of the binuclear iron complex **[Fe_2L(py)$_4$]** (all-low spin).

Thermogravimetric Analysis

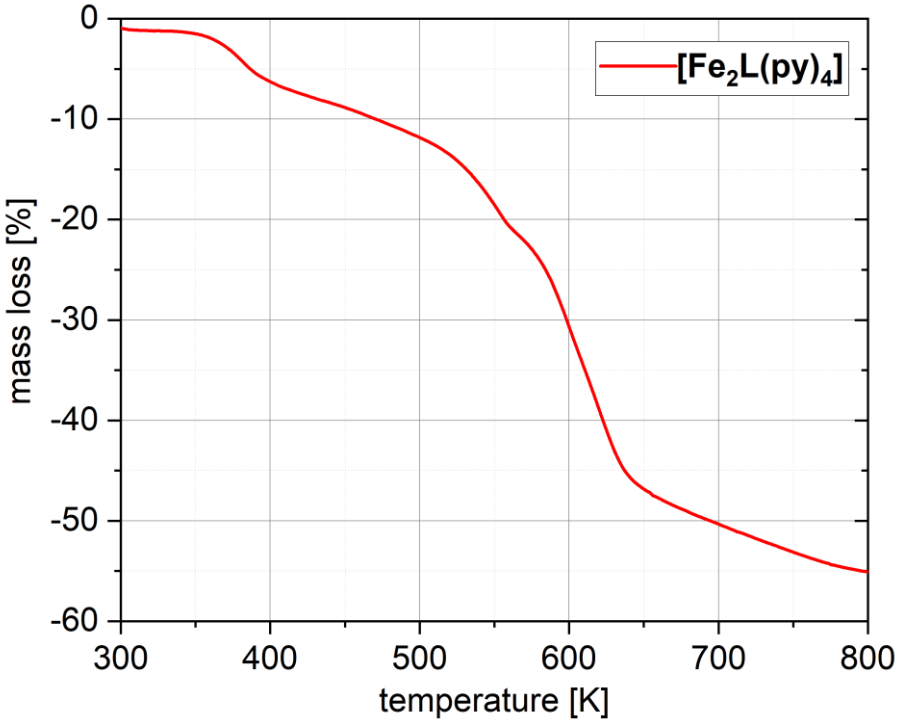

Figure S8: Thermogravimetric analysis of **[$Fe_2L(py)_4$]** under argon atmosphere.

UV-Vis absorption spectra

Spectral deconvolutions of the UV-Vis absorption spectra of H_4**L**, **[Ni_2L]**, **[Cu_2L]** and **[Fe_2L(py)$_4$]** are shown in Figure S 13. It is noted that the fit procedure was model-free; that is, the fit was phenomenological with no *a priori* physical meaning. While overall red-shifted spectra prevail for all metal complexes, only the copper complex retains the overall spectral shape of the ligand spectrum. The long-wavelength band fits to a single Gaussian profile, which is red-shifted by 2400 cm^{-1} with respect to the ligand spectrum. A very similar shift prevails for the near-UV band. The long-wave tailing of the strong Vis absorption in **[Cu_2L]** hides an additional, weak transition with a maximum at ca. 15.000 cm^{-1}, which is readily identified as the d^9 ligand-field absorption. In the case of nickel and iron the spectral shapes do no longer mimic the parent ligand spectrum. The long-wavelength band clearly consists of (at least) two strong individual transitions in both cases (in the fit, maxima are located at ν = 20.700 cm^{-1} and ν = 23.700 cm^{-1} and ν = 21.500 cm^{-1} and ν = 25.000 cm^{-1} for nickel and iron, respectively).

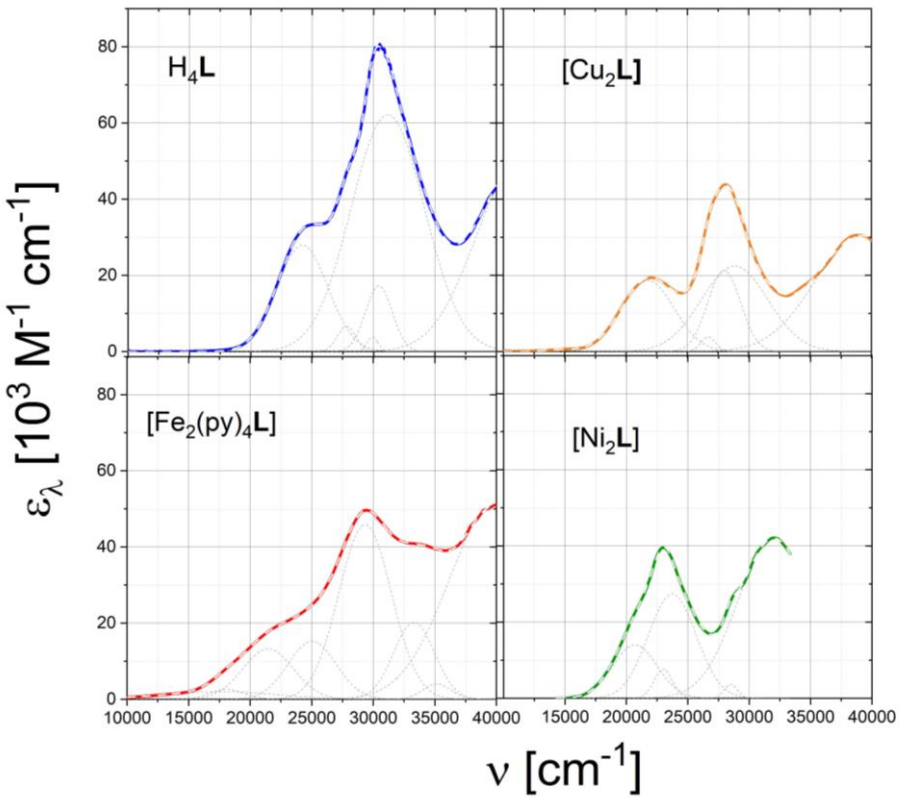

Figure S9: Gaussian deconvolution of the UV-Vis absorption spectra of H_4**L**, **[Ni_2L]**, **[Cu_2L]** and **[Fe_2L(py)$_4$]** (for Cu, the given molar absorption coefficients denote lower limits); colored line: exp. data; dottet: individual fit components; dashed: composite fit.

Magnetic Properties

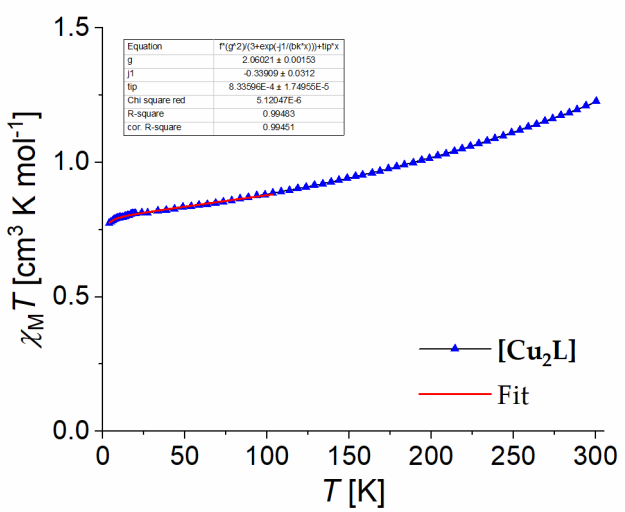

Figure S10: Temperature dependence of $\chi_M T$ of [Cu$_2$L], including a fit to the coupling model of Bleaney-Bowers.

^{57}Fe-Mössbauer Spectroscopy

Table S 5: ^{57}Fe Mössbauer parameters for all iron compounds.

Sample	T [K]	Site	species	δ [mm s^{-1}]	ΔE_Q [mm s^{-1}]	$\Gamma/2$ [mm s^{-1}]	Area [%]
[Fe$_2$L(py)$_4$]	298	D1	Fe(II) HS	0.99(4)	2.15(8)	0.41(5)	65(8)
		D2	Fe(II) LS	0.31(7)	1.19(15)	0.43(11)	35(8)
	200	D1	Fe(II) HS	1.01(4)	2.29(8)	0.13(4)	29(7)
		D2	Fe(II) LS	0.40(2)	1.20(5)	0.17(3)	71(8)
	100	D1	Fe(II) HS	1.10(4)	2.23(8)	0.14(6)	19(6)
		D2	Fe(II) LS	0.430(10)	1.132(19)	0.154(14)	81(5)
	80	D1	Fe(II) HS	1.104(13)	2.26(3)	0.14(2)	17.7(18)
		D2	Fe(II) LS	0.435(3)	1.148(6)	0.153(4)	82.3(17)
[Fe$_2$L(py)$_4$]^{heated}	150	D1	Fe(II) HS	1.02(3)	2.29(5)	0.18(4)	61(9)
		D2	Fe(II) LS	0.42(4)	1.27(9)	0.13(6)	25(14)
		D3	Fe(III) HS	0.41(6)	0.73(16)	0.13(11)	14(13)
	80	D1	Fe(II) HS	1.031(13)	2.31(3)	0.157(18)	65(5)
		D2	Fe(II) LS	0.42(3)	1.30(8)	0.14(5)	22(12)
		D3	Fe(III) HS	0.43(4)	0.78(12)	0.13(8)	13(11)
[Fe$_2$L(dmap)$_4$]	150	D1	Fe(II) HS	1.12(4)	2.29(8)	0.16(6)	24(6)
		D2	Fe(II) LS	0.423(12)	1.08(2)	0.161(16)	76(5)
	80	D1	Fe(II) HS	1.189(8)	2.305(17)	0.148(13)	15.5(10)
		D2	Fe(II) LS	0.4455(18)	1.082(4)	0.166(26)	84.5(10)
[Fe$_2$L(bpee)$_2$]$_n$	150	D1	Fe(II) HS	1.14(11)	2.2(2)	0.22(17)	12(7)
		D2	Fe(II) LS	0.407(10)	1.131(18)	0.166(14)	88(6)
	80	D1	Fe(II) HS	1.26(8)	2.21(16)	0.23(13)	13(6)
		D2	Fe(II) LS	0.424(7)	1.109(13)	0.156(10)	87(5)

Cyclic voltammograms

Table S 6: Measured half wave potentials $E_{1/2}$ [V] and their corresponding peak-to-peak seperations ΔE [V] of the investigated samples.

sample	solv	$E_{1/2}^1$	$E_{1/2}^2$	$E_{1/2}^3$	$E_{1/2}^4$	ΔE^1	ΔE^2	ΔE^3	ΔE^4	E^{1ox}	E^{1red}	E^{2ox}	E^{2red}	E^{3ox}	E^{3red}	E^{4ox}	E^{4red}
H_4**L**	DCM	0.665[a)]	0.321			0.145[a)]	0.186			0.737	0.592 0.504	0.414	0.228				
[Ni_2L]	DCM	0.697	0.263			0.087	0.067			0.740	0.653	0.296	0.229				
[Fe_2L(py)$_4$]	DCM		0.202		0.001		0.150		0.220		0.616	0.278	0.128	0.182		0.111	−0.109
H_4**L**	MeCN	0.578	0.300			0.189	0.105			0.672	0.483	0.352	0.247				
ox	DCM	0.640				0.088				0.684	0.596						

[a)]Appearance of two reduction peaks. Calculated $E_{1/2}$ and ΔE based on the first of two reduction peaks at 0.592 V.

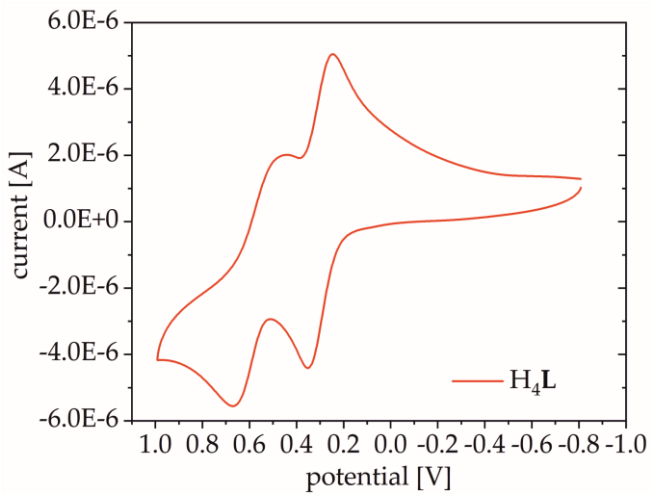

Figure S11: Cyclic voltammogram of a H_4**L**; measured in MeCN ($c = 1.0 \times 10^{-3}$ M) with NBu_4PF_6 ($c = 0.1$ M) on a platinum working and counter electrode with a saturated calomel reference electrode (SCE) and a scan rate of 50 mV s^{-1}. Potentials are reported in reference to Fc/Fc^+.

Chemical oxidation

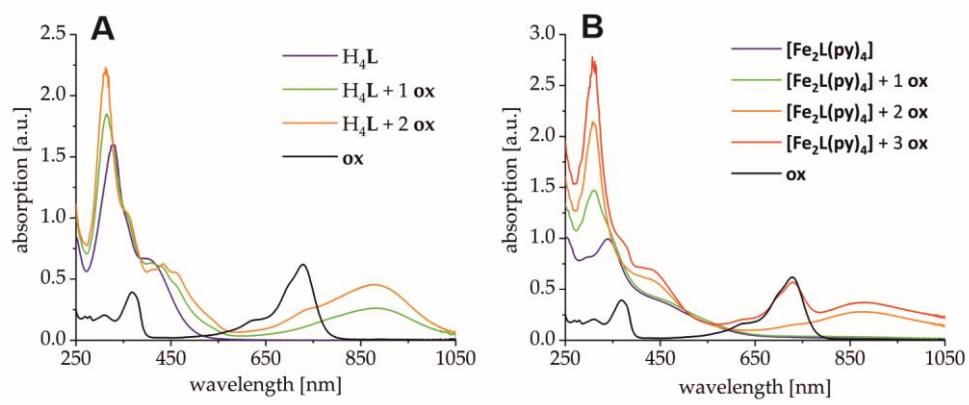

Figure S12: UV-Vis absorption spectra of (**A**) the ligand H_4**L** and (**B**) **[Fe_2L(py)$_4$]** in DCM after addition of varying amounts of oxidation agent $[N(C_6H_5Br\text{-}4)_3]^{+\bullet}$ $[\{3,5\text{-}(CF_3)_2C_6H_3\}_4B]^-$ ox; ($c = 2.0 \times 10^{-5}$ M).